Atmospheric
Measurement
Techniques

Open Access

Multispectral information from TANSO-FTS instrument – Part 1: Application to greenhouse gases (CO$_2$ and CH$_4$) in clear sky conditions

H. Herbin, L. C.-Labonnote, and P. Dubuisson

Laboratoire d'Optique Atmosphérique (LOA), UMR8518, Université de Lille 1, 59655 Villeneuve d'Ascq cedex, France

Correspondence to: H. Herbin (herve.herbin@univ-lille1.fr)

Abstract. The Greenhouse gases Observing SATellite (GOSAT) mission, and in particular the Thermal And Near infrared Sensor for carbon Observations–Fourier Transform Spectrometer (TANSO-FTS) instrument, has the advantage of being able to measure simultaneously the same field of view in different spectral ranges with a high spectral resolution. These features allow studying the benefits of using multispectral measurements to improve the CO$_2$ and CH$_4$ retrievals.

In order to quantify the impact of the spectral synergy on the retrieval accuracy, we performed an information content (IC) analysis from simulated spectra corresponding to the three infrared bands of TANSO-FTS. The advantages and limitations of using thermal and shortwave infrared simultaneously are discussed according to surface type and state vector composition. The IC is then used to determine the most informative spectral channels for the simultaneous retrieval of CO$_2$ and CH$_4$. The results show that a channel selection spanning the three infrared bands can improve the computation time and retrieval accuracy. Therefore, a selection of less than 700 channels from the thermal infrared (TIR) and shortwave infrared (SWIR) bands allows retrieving CO$_2$ and CH$_4$ simultaneously with a similar accuracy to using all channels together to retrieve each gas separately.

1 Introduction

The survey at global scale of greenhouse gases, in particular CO$_2$ and CH$_4$, takes advantage of the numerous space-borne infrared instruments. Work performed from high spectral measurements in the thermal infrared (TIR), such as AIRS (Crevoisier et al., 2003; Engelen and Stephens, 2004; Divakarla et al., 2006; Chahine et al., 2008; Maddy et al., 2008; Xiong et al., 2008), TES (Shepard et al., 2008; Kulawik et al., 2010; Worden et al., 2012) and IASI (Crevoisier et al., 2009; Herbin et al., 2009; Razavi et al.; 2009), has demonstrated the sensitivity of these observations to the mid-troposphere. Moreover, the OCO's pre-launch studies (Connor et al., 2008; Butz et al., 2009) as well as those from the shortwave infrared (SWIR) instrument SCIAMACHY (Buchwitz et al., 2005; Noël et al., 2005) have illustrated the ability of such measurements to get information on gaseous concentrations near the surface. Therefore, a retrieval exploiting the synergy between TIR and SWIR observations looks promising to reproduce the whole tropospheric gas profile distribution better.

Previous studies from Christi and Stephens (2004), Li et al. (2004), Cho and Staelin (2006), and Aires et al. (2011) have demonstrated that the use of simultaneous, but different, observations can improve the accuracy of the retrieved parameters. Nevertheless, the applications remain particularly sparse because using information from different instruments is notoriously difficult (collocation, field of view size and homogeneity). Moreover, measurements obtained by the same instrument at different spectral ranges have not yet been exploited, because such methodologies need to take into account other parameters such as spectral and radiometric band-to-band calibration and also the development of more complex algorithms, which are highly time-consuming.

The TANSO-FTS (Thermal And Near infrared Sensor for carbon Observations–Fourier Transform Spectrometer) instrument, which measures simultaneously one TIR and two SWIR spectral bands with the same field of view, represents a unique resource for testing the high-resolution multispectral approach suitability. Although the SWIR domain has been extensively used for greenhouse gas measurements (Morino et al., 2011; Yoshida et al., 2011, 2013; Crisp et al., 2012), the TIR has been less often employed (Saitoh et al., 2009), and to our knowledge, there is no study that exploits both spectral ranges.

In this study, we present for the first time the contribution of high-resolution multispectral measurements for an optimal retrieval of the greenhouse gases CO_2 and CH_4 in clear sky conditions. In particular, we discuss the interest of using two or three spectral bands simultaneously according to the surface type and state vector composition. This synergetic approach is evaluated from the three infrared bands of the TANSO-FTS instrument thanks to a new radiative transfer algorithm developed at the Laboratoire d'Optique Atmosphérique (LOA).

The structure of the paper is as follows: GOSAT mission and its two instruments are briefly described in Sect. 2. The forward model, state vector and error description are detailed in Sect. 3. Section 4 is dedicated to an information content analysis of the gaseous profiles in clear sky conditions. Section 5 demonstrates the interest of a channel selection spanning the three infrared bands. Finally, Sect. 6 summarizes our results and presents perspectives for future applications.

2　Instrument description

The Greenhouse gases Observing SATellite (GOSAT), launched on 23 January 2009 by JAXA, is designed to monitor the global CO_2 and CH_4 distributions from space. GOSAT is in a sun-synchronous orbit at 666 km altitude with three-day recurrence, and measures at around 13:00 local time. It is equipped with two instruments: the Thermal And Near infrared Sensor for carbon Observations–Fourier Transform Spectrometer (TANSO-FTS) and the Cloud and Aerosol Imager (TANSO-CAI). The TANSO-FTS performs high-spectral-resolution measurements ($0.2 \, cm^{-1}$, non-apodized) in the thermal infrared (TIR) (Band 4: 700–1800 cm^{-1}), shortwave infrared (SWIR) (Band 3: 4800–5200 and Band 2: 5800–6400 cm^{-1}) and visible (Band 1: 12 900–13 200 cm^{-1}) with an instantaneous field of view of 15.8 mrad, corresponding to a nadir circular footprint of about 10.5 km at ground level. For the SWIR and visible bands, the incident light is recorded as two (P and S) orthogonal polarization components. TANSO-CAI has four narrow bands from the near ultraviolet to near-infrared regions at 0.38, 0.674, 0.87, and 1.6 μm, with spatial resolutions of 0.5, 0.5, 0.5, and 1.5 km, respectively, for nadir pixels.

3　The multispectral TANSO-FTS simulation

3.1　The forward model

Accurate calculations of the radiances observed by TANSO-FTS are achieved with the high spectral resolution (up to $0.0001 \, cm^{-1}$) code LBLDOM (Dubuisson et al., 1996, 2005) over the thermal and solar spectral regions (0.2–16 μm). Radiances at the top of the atmosphere are calculated by solving the radiative transfer equation (RTE) in a horizontally homogeneous scattering atmosphere, using the discrete ordinate method (DOM) (Stamnes et al., 1988). Gaseous absorption is calculated with a line-by-line code based on STRANSAC (Scott, 1974) and the HITRAN 2008 database (Rothman et al., 2009). In this study, we assume a perfect filtering of the spectra containing cloud and aerosol observations. In the absence of atmospheric scattering, it is not necessary to use the O_2 A-Band (Band 1). Indeed, this band is mainly used to obtain an accurate optical path length when significant amount of scattering particles remains in the atmosphere. In this study the term "all bands" refers then to the use of Bands 2, 3 and 4 simultaneously. The absorption lines are computed at $0.01 \, cm^{-1}$ spectral resolution assuming a Voigt line shape. Absorption continua (H_2O, CO_2, and N_2) are also included from the MT-CKD parameterization (Clough et al., 2005). The solar irradiance database reported by Kurucz (http://kurucz.harvard.edu/sun/irradiance2008/) is used as the incident solar spectrum. Lambertian surface is assumed; thus the effect of surface polarization is disregarded. The albedo in the two SWIR bands is estimated from MODIS Terra product (Moody et al., 2008) and chosen as follows: desert and seawater in order to cover high and weak surface reflectivities, respectively. The corresponding surface emissivity for the TIR band is estimated from the MODIS UCSB library (http://www.icess.ucsb.edu/modis/EMIS/html/em.html). The only use of a nadir viewing angle, with a solar zenith angle of 30°, does not alter results or the discussion of the study, even if the sensitivity is correlated to viewing geometry.

Finally, the total intensity of TANSO-FTS spectra is simulated using the instrumental line shapes provided for each band by the GOSAT user interface gateway (https://data.gosat.nies.go.jp/gateway/gateway/MenuPage/open.do), and no post-apodization is applied, which allows the exploitation of the full spectral resolution.

Figure 1 illustrates the forward model capabilities to simulate the three infrared bands of TANSO-FTS in clear sky conditions. It shows an example of observed spectrum and the simulated individual contributions of major molecular absorbers on US standard profiles. Even if this instrument is mainly dedicated to CO_2 and CH_4 measurement, its instrumental qualities (spectral range, spectral resolution and signal-to-noise ratio) could enable detection of number of other species such as water vapor isotopologues HDO, $H_2^{18}O$ or $H_2^{17}O$ (see Fig. 1 and Frankenberg et al., 2013).
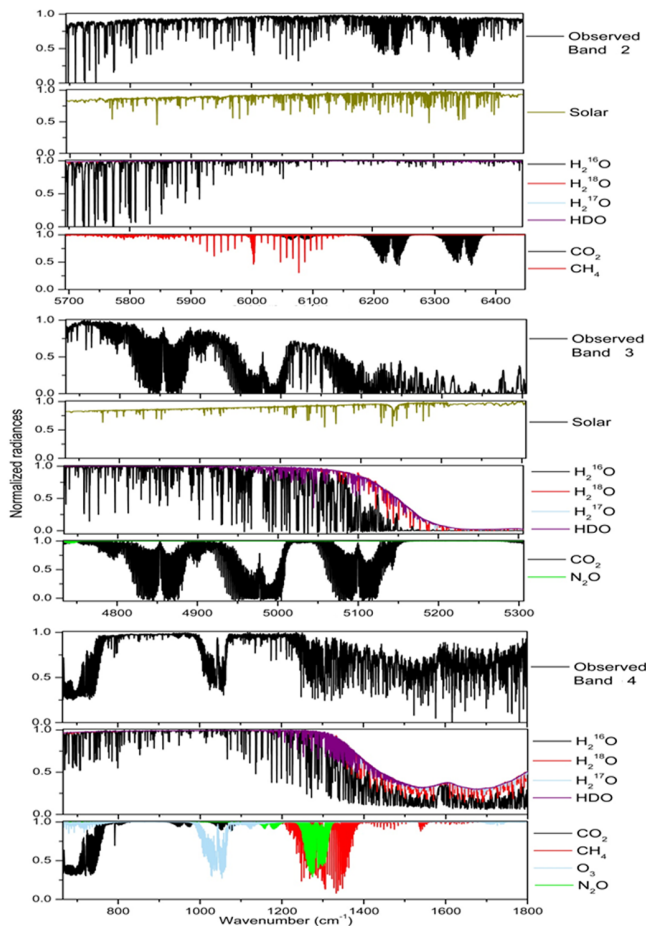
Fig. 1. Example of observed TANSO-FTS spectrum in normalized radiances, simulated solar contribution and individual major molecular absorbers. Each band is calculated from our line-by-line forward model on US standard profiles with nadir viewing angle and solar zenith angle of 30°.

3.2 Information content theory

In the case of an atmosphere divided in discrete layers, the forward radiative transfer equation gives an analytical relationship between the set of observations $\boldsymbol{y}$ (here, the radiances) and the vector of true atmospheric parameters $\boldsymbol{x}$ and is written as

$$\boldsymbol{y} = F(\boldsymbol{x}) + \varepsilon, \tag{1}$$

where F represents the model that allows mapping the state space to the measurement space, and ε the measurements and/or forward model error vector.

In the case of information content (IC) analysis, we do not need to introduce the whole optimal estimation theory formulation used for the retrieval described by Rodgers (2000). In this study, two matrices ($\mathbf{A}$ and $\mathbf{S}_x$) fully characterize the information provided by the observing system.

The first one is the averaging kernel matrix, $\mathbf{A}$, which gives a measure of the sensitivity of the retrieved state to the true state, defined by

$$\mathbf{A} = \partial \hat{\boldsymbol{x}} / \partial \boldsymbol{x} = \mathbf{GK}, \tag{2}$$

where $\mathbf{K}$ is the Jacobian matrix (or weighting function), the ith row of which is the partial derivatives of the ith measurement with respect to each (j) element of the state vector: $\mathbf{K}_{ij} = (\partial F_i / \partial \boldsymbol{x}_j)$, and $\mathbf{K}^{\mathrm{T}}$ is its transpose. $\mathbf{G}$ is the gain matrix, whose rows are the derivatives of the retrieved state with respect to the spectral points, defined by

$$\mathbf{G} = \partial \hat{\boldsymbol{x}} / \partial \boldsymbol{y} = (\mathbf{K}^{\mathrm{T}} \mathbf{S}_\varepsilon \mathbf{K} + \mathbf{S}_a^{-1})^{-1} \mathbf{K}^{\mathrm{T}} \mathbf{S}_\varepsilon^{-1}, \tag{3}$$

where $\mathbf{S}_a$ is the error covariance matrix describing our knowledge of the state space prior to the measurement and $\mathbf{S}_\varepsilon$ represents the forward model and the measured signal error covariance matrix.

At a given level, the peak of the averaging kernel row gives the altitude of maximum sensitivity, whereas its full width at half maximum is an estimate of the vertical resolution. Rodgers (2000) demonstrated that the trace of $\mathbf{A}$ represents the total degrees of freedom for signal (DOFSs), which indicates the amount of independent pieces of information provided by the observing system as regards as the state vector. In an ideal inverse method, the averaging kernel $\mathbf{A}$ would be the identity matrix representing a perfect retrieval with a DOFS equal to the size of the state vector. Consequently, each diagonal element of $\mathbf{A}$ is equivalent to partial degree of freedom attached to each element of the state vector (or attached to each parameter we want to retrieve).

The second essential matrix is the error covariance matrix $\mathbf{S}_x$, which describes our knowledge of the state space posterior to the measurement. Rodgers (2000) demonstrated that this error covariance matrix can be written as

$$\mathbf{S}_x = \left(\mathbf{S}_a^{-1} + \mathbf{K}^{\mathrm{T}} \mathbf{S}_\varepsilon^{-1} \mathbf{K}\right)^{-1}. \tag{4}$$

In this expression the matrix $\mathbf{S}_\varepsilon$ can be written as follows:

$$\mathbf{S}_\varepsilon = \mathbf{S}_{\mathrm{m}} + \mathbf{K}_b \mathbf{S}_b, \mathbf{K}_b^{\mathrm{T}} = \mathbf{S}_{\mathrm{m}} + \mathbf{S}_{\mathrm{f}}, \tag{5}$$

with $\mathbf{S}_b$ representing the error covariance matrix formed by the errors attached to non-retrieved model parameters, $\mathbf{S}_{\mathrm{f}}$ the forward model error covariance matrix, and $\mathbf{S}_{\mathrm{m}}$ the measured signal error covariance matrix. Therefore, we can estimate the contribution of the prior measurement and forward model error to the posterior error $\mathbf{S}_x$ as follows:

$$\mathbf{S}_{\mathrm{smoothing}} = (\mathbf{A} - \mathbf{I}) \mathbf{S}_a (\mathbf{A} - \mathbf{I})^{\mathrm{T}}. \tag{6}$$

The smoothing error covariance matrix $\mathbf{S}_{\mathrm{smoothing}}$ represents the vertical sensitivity of the measurements to the retrieved profile.

$$\mathbf{S}_{\mathrm{meas.}} = \mathbf{G} \mathbf{S}_{\mathrm{m}} \mathbf{G}^{\mathrm{T}}. \tag{7}$$

The contribution of the measurement error covariance matrix $\mathbf{S}_m$ to the posterior error covariance matrix $\mathbf{S}_x$ is given by $\mathbf{S}_{meas}$. $\mathbf{S}_m$ is computed from the spectral noise.

$$\mathbf{S}_{fwd.mod.} = \mathbf{G}\mathbf{K}_b\mathbf{S}_b(\mathbf{G}\mathbf{K}_b)^T = \mathbf{G}\mathbf{S}_f\mathbf{G}^T. \tag{8}$$

The forward model error covariance matrix $\mathbf{S}_f$ illustrates the imperfect knowledge of the non-retrieved model parameters, and its contribution to the posterior error covariance matrix is given by $\mathbf{S}_{fwd.mod.}$.

The total error covariance matrix can then be regarded as the sum of these individual contributions, and Eq. (4) can be rewritten as

$$\mathbf{S}_x = \mathbf{S}_{smoothing} + \mathbf{S}_{meas} + \mathbf{S}_{fwd.mod.}. \tag{9}$$

3.3 A priori information

The IC analysis uses simulated unpolarized intensity spectra of TANSO-FTS SWIR Bands 2 and 3, and TIR Band 4. The CO_2 and CH_4 vertical concentrations of the a priori state vector $\mathbf{x}_a$ are based on US standard profile discretized on 21 vertical levels, extending from the ground to 20 km height with 1 km step. In addition, the humidity and temperature profile, surface reflectivity, and the TIR surface emissivity are included in the non-retrieved parameters and will be discussed in detail in Sect. 3.4. The a priori values and their a priori variabilities are summarized in Table 1 and described subsequently hereafter.

3.3.1 A priori error covariance matrix

The a priori error covariance matrix $\mathbf{S}_a$ can be evaluated from climatology or in situ data. Nevertheless, the off-diagonal matrix elements increase the correlation of the vertical layers. Since this study is dedicated to information coming from the measurement rather than climatological or in situ observations, we will always assume $\mathbf{S}_a$ as a diagonal matrix with the ith diagonal element $(S_{a,ii})$ defined as

$$S_{a,ii} = \sigma_{a,i}^2 \quad \text{with} \quad \sigma_{a,i} = x_{a,i} \cdot \frac{p_{error}}{100}, \tag{10}$$

where $\sigma_{a,i}$ stands for the standard deviation in the Gaussian statistics formalism. The subscript i represents the ith parameter of the state vector.

The CO_2 profile a priori error (red line of Fig. 2) is estimated from Schmidt and Khedim (1991) and is very similar to the one used by Christi and Stephens (2004). The CH_4 a priori error is fixed to $P_{error} = 5\%$, which corresponds to an under-constrained version of the error covariance matrix used by Razavi et al. (2009) and Frankenberg et al. (2012).

3.3.2 Measurement error covariance matrix

In order to compute the measurement error covariance matrix, one needs to know the instrument performance or accuracy. The instrument performance corresponds to the radiometric calibration (which could be a bias) and radiometric

noise, usually given as signal-to-noise ratio (SNR). This error covariance matrix is assumed to be diagonal, and the ith diagonal element can be computed as follows:

$$S_{m,ii} = \sigma_{m,i}^2 \quad \text{with} \quad \sigma_{m,i} = \frac{y_i}{SNR}, \tag{11}$$

where $\sigma_{m,i}$ is the standard deviation of the ith measurement (y_i) of the measurement vector $\mathbf{y}$, representing the noise equivalent spectral radiance. For the TIR Band 4, the SNR is estimated as 300 for a 280 K blackbody light input (Kuze et al., 2009). For the SWIR bands, there are two main noise sources: (1) the detector and electronics noise, which is independent of the signal intensity and (2) the shot noise, which is proportional to the square root of the total amount of input light. Because of the wide spectral range of Band 2, the main contribution to the total noise comes therefore from the shot noise. However, we have applied an identical SNR for Bands 2 and 3. The latter is estimated from the Band 2 SNR values given by Yoshida et al. (2011). According to the different surface types, the SNR was set to 500, and 150 representative of our high (desert-like), and low (seawater-like) surface reflectivity cases.

3.4 Non-retrieved parameter characterization and accuracy

Evaluation of the forward model accuracy is the most difficult part of the error description. Indeed, it consists in both the model precision (for example 1-D approximation, Lambertian surface, accuracy of the computation) as well as the error due to the non-retrieved parameters $(\mathbf{x}_b)$ used in the forward model (e.g., temperature profile, ground emissivity, gas profile when they are not retrieved). As horizontal variability of gas and aerosol are small enough on a GOSAT pixel size, and as it is beyond the scope of this paper to explore 3-D effects due to horizontal sub-pixel heterogeneity, we choose to neglect it in this study. Thus, only effects of non-retrieved parameters uncertainties are explored here. Moreover, a vertically uniform uncertainty is assumed.

The most important variables when dealing with infrared measurements such as TANSO-FTS Band 4 are the temperature profile and surface temperature. We assume a realistic uncertainty, compatible with the typical values used for the ECMWF assimilation, of 1 K $(\Delta T = 1\,\text{K})$ on each layer of the temperature profile as well as on surface temperature. The contribution to the ith diagonal element of the forward model error covariance matrix can be computed as

$$\sigma_{f,T_j,i} = \frac{\partial F_i}{\partial T_j} \Delta T, \tag{12}$$

where j stands for the jth level and i for the ith measurement.

The surface emissivity (ε_m) uncertainty is set to $P_{\varepsilon_m} = 2\%$, which corresponds to an average value of the albedo absolute accuracy from MODIS and IASI (Capelle et al., 2012),

Table 1. State vector parameters.

State vector elements	H_2O	CO_2	CH_4	Interfering species	Surface temperature	Profile temperature	Emissivity/ reflectivity
A priori values ($\boldsymbol{x}_a$)	US standard						MODIS database
A priori uncertainty (P_{error})	10 %	1.3–8 %	5 %	100 %	1 K	1 K/layer	2 %

and its contribution to the ith diagonal element of the forward model error covariance matrix is

$$\sigma_{\text{f},\varepsilon,i} = \frac{\partial F_i}{\partial \varepsilon} \Delta\varepsilon, \quad \text{with} \quad \Delta\varepsilon = \frac{p_{\varepsilon_m}}{100} \varepsilon_m. \tag{13}$$

We assumed a very poor knowledge on the interfering molecule concentration with an uncertainty ($P_{C\text{mol}}$) of 100 %, and as before their contribution to the ith diagonal element of the forward model error covariance matrix can be computed as

$$\sigma_{\text{f},C_{\text{mol}^k},i} = \frac{\partial F_i}{\partial c_{\text{mol}^k}} \Delta c_{\text{mol}^k}, \quad \text{with} \quad \Delta c_{\text{mol}^k} = \frac{p_{C\text{mol}}}{100} c_{\text{mol}^k}, \tag{14}$$

where C_{mol^k} represents the concentration of the kth interfering molecule.

If H_2O is treated as a non-retrieved molecule and is assumed to be known from ancillary data, its a priori error profile is set to $P_{CH_2O} = 10\,\%$. This error value is compatible with typical a posteriori uncertainties from operational Level 2 products of a dedicated instrument such as IASI (Clerbaux et al., 2007).

Finally, the total forward model error covariance matrix ($\mathbf{S}_\text{f}$), assumed diagonal in the present study, is given by summing all the previous contributions for each diagonal element, and the ith diagonal element ($S_{\text{f},ii}$) is given by

$$S_{\text{f},ii} = \sum_{j=1}^{n\text{level}} \sigma_{\text{f},T_j,i}^2 + \sum_{k=1}^{n\text{molecules}} \sigma_{\text{f},c_{\text{mol}^k},i}^2 + \sigma_{b,\varepsilon,i}^2. \tag{15}$$

Here, we did not consider the spectroscopic line parameter, line-mixing, continua or calibration errors.

4 Information content analysis applied to greenhouse gas profiles in clear atmosphere

In order to quantify the benefit of multispectral synergy, it is essential to perform, first, an information content analysis on CO_2, and CH_4 profiles separately (Case 1). By separately we mean that the state vector is constituted of only one of the above gas concentrations at each level between 0 and 20 km. This corresponds to the case where we estimated each gas profile alone when all other atmospheric parameters and all other gas profiles are assumed to be known from ancillary data with a specific variability or uncertainty.

Figures 2 and 3 show the averaging kernel $\mathbf{A}$ and total posterior error $\mathbf{S}_x$ for CO_2 and CH_4, respectively, and for each surface type. $\mathbf{A}$ is obtained for each greenhouse gas independently using the variability introduced in the previous section and considering an observing system composed of Band 2, 3 or 4 alone and all the bands together. Each colored line represents the row of $\mathbf{A}$ at each vertical grid layer. The blue circles represent the partial degree of freedom of the gas at each level (diagonal element of $\mathbf{A}$). The latter indicates the proportion of information provided by the measurement. Indeed, a value close to unity means that the information mainly comes from the measurement, while a value close to zero indicates that the information is strongly related to the a priori.

For both surface types, Fig. 2 shows that most of the information about CO_2 arises from the ground to 10 km high in the atmosphere, while at upper altitude the error is mainly governed by the a priori uncertainty, due to a smaller sensitivity to CO_2 in the upper troposphere. In the lower part of the atmosphere, the a posteriori total error (black line) is significantly weaker than the a priori error (red line). The vertical distribution of $\mathbf{A}$ illustrates the sensitivity to CO_2 in the lower atmosphere (0–3 km) from SWIR bands. Nevertheless, this sensitivity dramatically decreases with the surface albedo to be almost insignificant above seawater. This phenomenon is well known, and the operational Level 2 products from TANSO-FTS (Yoshida et al., 2011, 2013) treat only the spectra over ocean where the specular reflection occurs and reflectance is high. The TIR sensitivity in the mid-troposphere (3–10 km) is less influenced by the surface characteristics (see panels Band 4 from Fig. 2) and appears to be very suitable to retrieve CO_2 abundances when the surface albedo is weak. The most important result of Fig. 2 is the improvement of the vertical information distribution when we use all the bands simultaneously, in particular, when the reflectivity is significant. For instance, in the case of desert surface, the total DOFSs are 0.75, 1.16, 1.32 and 2.59, for Band 2, 3, 4 and all the bands respectively. The latter show that one might be able to retrieve between 2 and 3 partial tropospheric columns for CO_2. Nevertheless, the CO_2 error is always dominated by the a priori error, which means that the information is strongly constrained by the a priori profile and little information is introduced from the measurement. Therefore, even with a high a priori constraint on the CO_2 profile, this study shows that using all the TANSO-FTS bands together leads to an improvement of the a posteriori
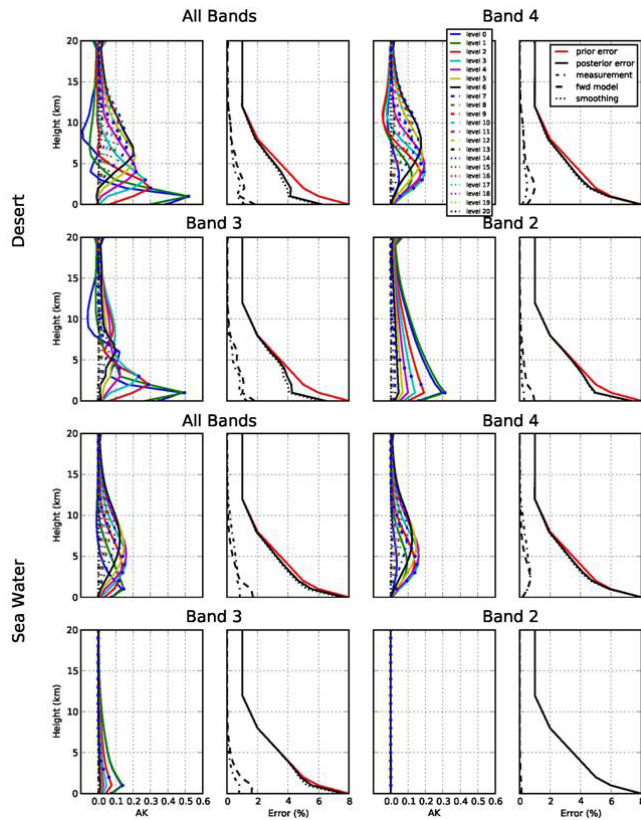
Fig. 2. Averaging kernels and error budgets of CO_2 vertical profiles for Bands 2, 3, and 4 separately and all the bands together in Case 1. the red and black lines stand for the prior ($\mathbf{S}_a$) and posterior ($\mathbf{S}_x$) errors, respectively; the smoothing ($\mathbf{S}_{\text{smoothing}}$), model parameters ($\mathbf{S}_{\text{fwd.mod.}}$), and measurement ($\mathbf{S}_{\text{meas.}}$) errors are dotted, dashed, and dashed/dotted lines, respectively. The averaging kernels of each altitude layer are represented by different colors.

Fig. 3. Same as Fig. 2, but for CH_4.

error profile on CO_2 concentration, especially in the lower part of the atmosphere.

These results are close to those from previous studies (Christi and Stephens, 2004; Connor et al., 2008; Saitoh et al., 2009; Yoshida et al., 2011), but it is important to note that the absolute values of averaging kernel and error profile cannot be directly compared, since they depend on several parameters: (1) a priori values $\boldsymbol{x}_a$ and $\boldsymbol{x}_b$, (2) the variability of the error covariance matrix $\mathbf{S}_a$, $\mathbf{S}_f$ and $\mathbf{S}_m$, as well as (3) the vertical grid. The latter can be circumvented if the tropospheric column error (S_{XCO_2}) is derived from the vertical profile error as in Yoshida et al. (2011):

$$\sigma_{\text{XCO}_2} = \frac{\sqrt{\mathbf{C}_{\text{air}}^{\text{T}} \mathbf{S}_{\text{XCO}_2} \mathbf{C}_{\text{air}}}}{\mathbf{C}_{\text{air}}^{\text{T}} \mathbf{1}}, \tag{16}$$

where $\mathbf{C}_{\text{air}}$ is the vector containing the air molecule concentration at each level, and $\mathbf{1}$ is a column vector with unity elements.
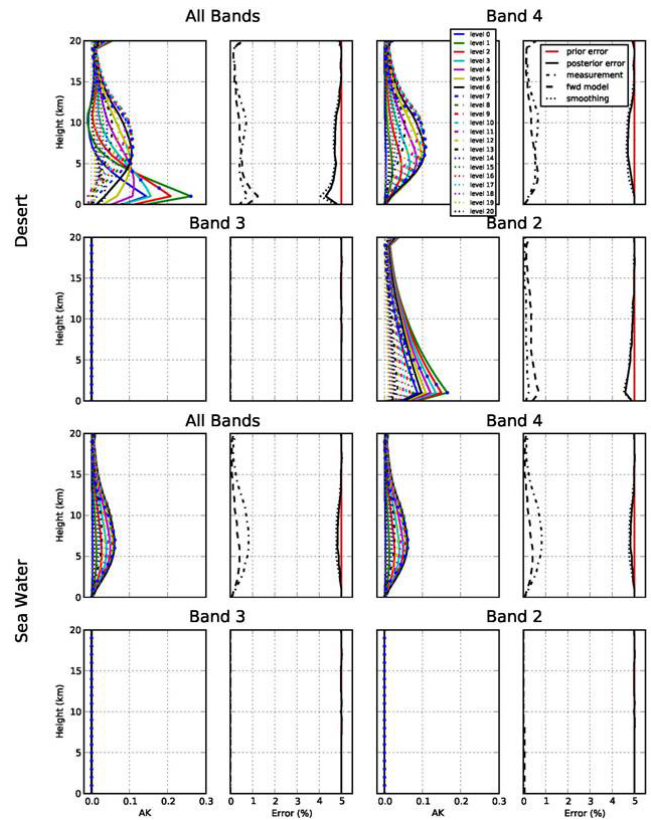
The CO_2 total column posterior error is estimated to be less than 1.2 % whatever the surface (see Table 2), which is comparable to the results from previously mentioned studies.

As for CO_2, Fig. 3 shows that the general conclusion is identical for CH_4 but with a smaller information content. Because it does not contain any methane absorption lines, Band 3 shows no information (see Figs. 1 and 3). For the remaining bands, the $\mathbf{A}$'s are broader than those of CO_2, suggesting a very important correlation between layers and then a degradation of the vertical resolution. Moreover, Band 2 becomes unusable for small surface albedo values (see seawater panel of Fig. 3). For comparison with CO_2, in the case of desert, the total DOFSs are 0.64, 0.84 and 1.63, for Band 2, 4 and all the bands respectively. These weak values highlight the difficulty in retrieving more than one or two tropospheric columns of methane from such measurements.

As a general trend, the simultaneous use of all the bands together instead of Band 4 alone (TIR) or Band 2 and 3 (SWIR) increases the total DOFS and reduces systematically the total errors of the two gas species. Band 4 has the advantage of providing mid-tropospheric information weakly affected by the surface albedo. The SWIR bands have the advantage of having low measurement and non-retrieved parameter errors (dashed and dotted lines in Figs. 2 and 3). This effect is mainly due to weak temperature dependence and

Table 2. Total DOFSs and column errors of CO_2 and CH_4 for each surface using all spectral channels.

	Desert		Seawater	
	DOFS	Errors (%)	DOFS	Errors (%)
CO_2 only (Case 1)	2.59	1.02	1.17	1.20
CO_2 with CH_4 (Case 2)	2.87	1.00	1.18	1.19
CH_4 only (Case 1)	1.63	1.26	0.51	1.34
CH_4 with CO_2 (Case 2)	1.65	1.25	0.52	1.33
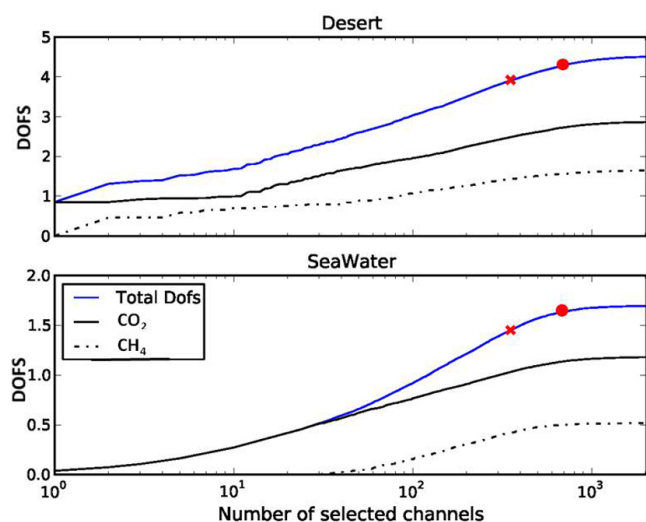
Fig. 4. Evolution of the DOFSs with number of selected channels for CO_2 (solid black line) and CH_4 (black dashed line) separately, and all together (blue line). The red crosses and circles symbolize the number of channels (355 and 694) corresponding to 75 % and 90 % of the total IC.

less interference from other molecules in the SWIR. Moreover, in the case of high reflectance, the sensitivity to CO_2 and CH_4 concentrations is comparable to TIR spectral range, but centered in the lower troposphere, where variability of greenhouse is the most important.

In the operational GOSAT level 2 products, both CO_2 and CH_4 gas concentrations are obtained simultaneously (Yoshida et al., 2011). Therefore, we investigate how the inclusion of CO_2 and CH_4 profiles in the same state vector could improve the information content (this case will be refereed as Case 2 hereafter). All the a priori values and variabilities are the same as in the previous section (see Table 1).

Although the differences with the results from the previous section are rather small, we can observe a significant effect over bright surface (e.g., desert) in the lower atmosphere where the sensitivity is higher. The averaging kernels (not shown here) appear to be narrower with strongest amplitude involving a better vertical resolution, especially from the ground up to 5 km. Table 2 summarizes the CO_2 and CH_4 total DOFS and total column errors for all cases, each gas individually (Case 1) or together (Case 2) in the state vector.

The latter illustrates how a state vector including both gases enhances the total information. However, even if the total information is better, the impact on the total errors seems limited, due to the high constraint on each a priori gas profile. Nevertheless, we can conclude that taking into account CO_2 and CH_4 together in the state vector involves an improvement of their accuracy retrievals. Obviously, this improvement is driven by the relative amount of information coming from the measurement in regard to the a priori and non-retrieved parameter uncertainties. This improvement is weak (cf. Table 2) for CO_2 and CH_4. Therefore, the benefit of simultaneous retrieval depends on the additional computing time generated (see following section).

5 Channel selection

Using all channels, measured by TANSO-FTS, in the retrieval scheme has two disadvantages. Firstly, it requires a very large computational time. This problem could be circumvented with optimized parallel programming and exploitation of the latest computer technologies such as GPU (Huang et al., 2011). Secondly, it increases the systematic error from correlation of the interfering species. In this case, a good evaluation of the a priori state vector x_a and error covariance matrix S_a is very challenging. As emphasized by Rodgers (2000), the IC framework is very well suited to optimize the selection of channels that carry the greatest amount of information. This procedure is well described in L'Ecuyer et al. (2006) and will not be developed in this paper. Previous studies already used channel selection to optimize the greenhouse gas retrievals from high-resolution infrared sounders. We can cite, for instance, the study of Dudhia et al. (2002) from the MIPAS spectra, or the works of Crevoisier et al. (2003) and Worden et al. (2004) from AIRS and TES respectively. Specifically applied to TANSO-FTS, Saitoh et al. (2009) developed a retrieval algorithm to retrieve CO_2 vertical profiles using the TIR (Band 4), and Kuai et al. (2010) discussed the practical advantages of channel selection in the SWIR bands (Band 2 and 3). The goal of this section is therefore to present results of a channel selection in order to reach a reasonable amount of information on both CO_2 and CH_4 columns using measurements from the TIR and SWIR spectral range simultaneously (Bands 4, 3 and 2).

Table 3. Number of selected channels.

	Desert		Seawater		All surfaces	
	75 %	90 %	75 %	90 %	75 %	90 %
CO_2 (Case 1)	118	320	139	259	227	468
CH_4 (Case 1)	65	151	117	196	151	248
$CO_2 + CH_4$ (Case 2)	209	520	239	446	355	694

Table 4. Band-by-band distribution (in %) of the selected channels in Case 2.

	CO_2 Desert		CO_2 Seawater		CH_4 Desert		CH_4 Seawater		$CO_2 + CH_4$ Desert		$CO_2 + CH_4$ Seawater		All gases All surfaces	
	75 %	90 %	75 %	90 %	75 %	90 %	75 %	90 %	75 %	90 %	75 %	90 %	75 %	90 %
Band 2	0	4	0	0	49	34	0	0	15	10	0	0	9	7
Band 3	64	63	8	17	0	0	0	0	40	40	6	12	27	35
Band 4	36	33	92	83	51	66	100	100	45	50	94	88	64	58

Table 5. Total DOFSs and column errors (%) of CO_2 and CH_4 for each surface from different amounts of selected channels.

	DOFS CO_2		ΣXCO_2 (%)		DOFS CH_4		ΣXCH_4 (%)	
	Desert	Seawater	Desert	Seawater	Desert	Seawater	Desert	Seawater
Channels								
2032 (Case 1)	2.59	1.17	1.02	1.20	1.63	0.51	1.26	1.34
2032 (Case 2)	2.87	1.18	1.00	1.19	1.65	0.52	1.25	1.33
355 (Case 2)	2.40	1.00	1.04	1.22	1.36	0.35	1.27	1.35
694 (Case 2)	2.67	1.13	1.02	1.21	1.57	0.47	1.26	1.34

Figure 4 presents the CO_2 and CH_4 total DOFS evolutions as a function of the number of selected channels from all spectral bands and for each surface type. The maximum number of selected channels has been fixed to 2032, which corresponds to all the channels from both 1.61 and 2.06 µm CO_2 bands used by Kuai et al. (2010). The first highlight coming from Fig. 4 is that the DOFS magnitude and evolution are strongly correlated to the surface type. Moreover, for each gas, the DOFS increases sharply with the first selected channels and then more steadily. This is perfectly illustrated in Table 3, which gives the number of channels required to reach 75 % and 90 % of the total information provided by using all the channels, for each gas and surface type. The distributions (in %) by spectral band of the previous selected channels are reported in Table 4. The TIR band (Band 4) appears predominant when the surface reflectivity is weak, whereas over bright surface SWIR bands (Band 2 and 3) become more important for CH_4 and preponderant for CO_2 (Table 4). Finally, the results from Table 4 demonstrate the usefulness of the multispectral information to retrieve the greenhouse gas concentrations with good accuracy for all the surface types.

Table 5 shows DOFSs and total errors, for different amounts of selected channels. As previously stated, Case 1 is related to the treatment of each gas separately and Case 2 when both gases are treated simultaneously. The different values of DOFSs and column errors confirm the retrieval improvement for each gas when they are treated simultaneously (see previous section). Obviously, the best information is provided by the use of all the available channels in Case 2 (see Table 2). However, the reduction to 2032 selected channels (Yoshida et al., 2011) does not affect the accuracy of the retrieved CO_2 and CH_4 columns. Moreover, a retrieval scheme that uses selected channels corresponding to 75 % or 90 % of the total information content would give comparable errors to a retrieval scheme using the entire set of channels. These results point out the interest of determining an optimal set of channels for each gas separately, and using this selection to retrieve these two gases simultaneously (see lines 355 and 694 of Table 5).

6 Summary and conclusion

To summarize, this study investigates the interest of retrieving greenhouse gas profiles from multispectral measurement. First, we performed an information content analysis on CO_2 and CH_4 separately in clear sky conditions from the TIR and SWIR bands of the TANSO-FTS instrument. We showed that

by using all the available channels, one might be able to retrieve between 1 and 2 partial columns for CH_4, and 2 or 3 for CO_2 from the ground to 20 km, demonstrating the interest of the spectral synergy. Assuming one single column leads to posterior errors better than 1.4 % and 1.2 %, for CH_4 and CO_2 respectively. Moreover, merging the CO_2 and CH_4 profiles in the same state vector implies a small improvement of a posteriori uncertainties and DOFSs. However, the impact on the tropospheric column errors of CO_2 and CH_4 appears rather weak because of the high constraint assumed on the a priori gas profile.

Finally, we showed that a selection of less than 700 channels from the three spectral bands allows retrieving CO_2 and CH_4 simultaneously with a comparable accuracy than using all channels to retrieve each gas separately.

Therefore, this study demonstrates that the most efficient way to retrieve CO_2 and CH_4 is to perform a channel selection across all the spectral bands for CO_2 and CH_4 separately for different surface types and to use all selected channels to retrieve both gases simultaneously.

This first paper is dedicated to an information content analysis on greenhouse gases (CO_2 and CH_4) from multispectral infrared measurements in clear sky conditions. Nevertheless, it is well known that the main source of errors is related to the presence of scattering particles. The second paper will therefore address this problem by studying (1) the aerosol information content using the four bands (from TIR to visible) of TANSO-FTS instrument and (2) their impact on the greenhouse gas retrievals.

References

Aires, F., Paul, M., Prigent, C., Rommen, B., and Bouvet M. : Measure and exploitation of multisensor and multiwavelength synergy for remote sensing: 2. Application to the retrieval of atmospheric temperature and water vapor from MetOp, Geophys. Res., 116, D02302, doi:10.1029/2010JD014702, 2011.

Buchwitz, M., de Beek, R., Burrows, J. P., Bovensmann, H., Warneke, T., Notholt, J., Meirink, J. F., Goede, A. P. H., Bergamaschi, P., Körner, S., Heimann, M., and Schulz, A.: Atmospheric methane and carbon dioxide from SCIAMACHY satellite data: initial comparison with chemistry and transport models, Atmos. Chem. Phys., 5, 941–962, doi:10.5194/acp-5-941-2005, 2005.

Butz, A., Hasekamp, O. P., Frankenberg, C., and Aben, I.: Retrievals of atmospheric CO_2 from simulated space-borne measurements of backscattered near-infrared sunlight: accounting for aerosol effects, Appl. Optics, 48, 3322–3336, 2009.

Cappelle, V., Chédin, A., Péquignot, E., Schlüssel, P., Newman, S. M., and Scott, N. A.: Infrared Continental Surface Emissivity Spectra and Skin Temperature Retrieved from IASI Observations over the Tropics, J. Appl. Meteorol. Climat., 51, 1164–1179, 2012.

Chahine, M. T., Chen, L., Dimotakis, P., Jiang, X., Li, Q., Olsen, E. T., Pagano, T., Randerson, J., and Yung, Y. L.: Satellite remote sounding of mid-tropospheric CO_2, Geophys. Res. Lett., 35, L17807, doi:10.1029/2008GL035022, 2008.

Cho, C. and Staelin, D. H.: Cloud clearing of Atmospheric Infrared Sounder hyperspectral infrared radiances using stochastic methods, J. Geophys. Res., 111, D09S18, doi:10.1029/2005JD006013, 2006.

Christi, M. J. and Stephens, G. L.: Retrieving profiles of atmospheric CO_2 in clear sky and in the presence of thin cloud using spectroscopy from the near and thermal infrared: A preliminary case study, J. Geophys. Res., 109, D04316, doi:10.1029/2003JD004058, 2004.

Clerbaux, C., Hadji-Lazaro, J., Turquety, S., George, M., Coheur, P.-F., Hurtmans, D., Wespes, C., Herbin, H., Blumstein, D., Tournier, B., and Phulpin, T.: The IASI/MetOp mission: first observations and highlight of its potential contribution to the GMES Earth observation component, Space Res. Today, 168, 19–24, 2007.

Clough, S. A., Shephard, M. W., Mlawer, E. J., Delamere, J. S., Iacono, M. J., Cady-Pereira, K., Boukabara, S., and Brown, P. D.: Atmospheric radiative transfer modeling: a summary of the AER codes, J. Quant. Spectrosc. Radiat. Transfer, 91, 233–244, 2005.

Connor, B., Boesch, H., Toon, G., Sen, B., Miller, C., and Crisp, D.: Orbiting Carbon Observatory: Inverse method and prospective error analysis, J. Geophys. Res., 113, D05305, doi:10.1029/2006JD008336, 2008.

Crevoisier, C., Chédin, A., and Scott, N. A.: AIRS channel selection for CO_2 and other trace-gas retrievals, Q. J. Meteorol. Soc., 129, 2719–2740, 2003.

Crevoisier, C., Chédin, A., Matsueda, H., Machida, T., Armante, R., and Scott, N. A.: First year of upper tropospheric integrated content of CO_2 from IASI hyperspectral infrared observations, Atmos. Chem. Phys., 9, 4797–4810, doi:10.5194/acp-9-4797-2009, 2009.

Crisp, D., Fisher, B. M., O'Dell, C., Frankenberg, C., Basilio, R., Bösch, H., Brown, L. R., Castano, R., Connor, B., Deutscher,

N. M., Eldering, A., Griffith, D., Gunson, M., Kuze, A., Mandrake, L., McDuffie, J., Messerschmidt, J., Miller, C. E., Morino, I., Natraj, V., Notholt, J., O'Brien, D. M., Oyafuso, F., Polonsky, I., Robinson, J., Salawitch, R., Sherlock, V., Smyth, M., Suto, H., Taylor, T. E., Thompson, D. R., Wennberg, P. O., Wunch, D., and Yung, Y. L.: The ACOS CO_2 retrieval algorithm – Part II: Global X_{CO_2} data characterization, Atmos. Meas. Tech., 5, 687–707, doi:10.5194/amt-5-687-2012, 2012.

Divakarla, M. G., Barnet, C. D., Goldberg, M. D., McMillin, L. M., Maddy, E., Wolf, W., Zhou, L., and Liu, X.: Validation of Atmospheric Infrared Sounder temperature and water vapor retrievals with matched radiosonde measurements and forecasts, J. Geophys. Res. 111, D09S15, doi:10.1029/2005JD006116, 2006.

Dubuisson, P., Buriez, J. C., and Fouquart, Y.: High spectral resolution solar radiative transfer in absorbing and scattering media: Application to the satellite simulation, J. Quant. Spectrosc. Radiat. Transfer, 55, 103–126, 1996.

Dubuisson P., Giraud, V., Chomette, O., Chepfer, H., and Pelon, J.: Fast radiative transfer modeling for infrared imaging radiometry, J. Quant. Spectrosc. Radiat. Transfer, 95, 201–220, 2005.

Dudhia, A., Jay, V., and Rodgers, C. D.: Microwindow selection for high- spectral-resolution sounders, Appl. Optics, 41, 3665–3673, 2002.

Engelen, R. J. and Stephens, G. L.: Information Content of Infrared Satellite Sounding Measurements with Respect to CO_2, J. Appl. Meteor., 43, 373–378, 2004.

Frankenberg, C., Hasekamp, O., O'Dell, C., Sanghavi, S., Butz, A., and Worden, J.: Aerosol information content analysis of multi-angle high spectral resolution measurements and its benefit for high accuracy greenhouse gas retrievals, Atmos. Meas. Tech., 5, 1809–1821, doi:10.5194/amt-5-1809-2012, 2012.

Frankenberg, C., Wunch, D., Toon, G., Risi, C., Scheepmaker, R., Lee, J.-E., Wennberg, P., and Worden, J.: Water vapor isotopologue retrievals from high-resolution GOSAT shortwave infrared spectra, Atmos. Meas. Tech., 6, 263–274, doi:10.5194/amt-6-263-2013, 2013.

Herbin, H., Hurtmans, D., Clerbaux, C., Clarisse, L., and Coheur, P.-F.: $H_2^{16}O$ and HDO measurements with IASI/MetOp, Atmos. Chem. Phys., 9, 9433–9447, doi:10.5194/acp-9-9433-2009, 2009.

Huang, B., Mielikainen, J., Oh, H., and Huang, H.-L. A.: Development of a GPU-based high-performance radiative transfer model for the Infrared Atmospheric Sounding Interferometer (IASI), J. Comput. Phys., 230, 2207–2221, 2011.

Kuai, L., Natraj, V., Shia, R.-L., Miller, C., and Yung, Y. L.: Channel selection using information content analysis: A case study of CO_2 retrieval from near infrared measurements, J. Quant. Spectrosc. Radiat. Transfer, 111, 1296–1304, 2010.

Kulawik, S. S., Jones, D. B. A., Nassar, R., Irion, F. W., Worden, J. R., Bowman, K. W., Machida, T., Matsueda, H., Sawa, Y., Biraud, S. C., Fischer, M. L., and Jacobson, A. R.: Characterization of Tropospheric Emission Spectrometer (TES) CO_2 for carbon cycle science, Atmos. Chem. Phys., 10, 5601–5623, doi:10.5194/acp-10-5601-2010, 2010.

Kuze, A., Suto, H., Nakajima, M., and Hamazaki, T.: Thermal and near infrared sensor for carbon observation Fourier-transform spectrometer on the Greenhouse Gases Observing Satellite for greenhouse gases monitoring, Appl. Optics, 48, 6716–6733, 2009.

L'Ecuyer, T. S., Gabriel, P., Leesman, K., Cooper, S. J., and Stephens, G. L.: Objective assessment of the information content of visible and infrared radiance measurements for cloud microphysical property retrievals over the global oceans. Part I: Liquid clouds, J. Appl. Meteor. Climatol, 45, 20–41, 2006.

Li, J., Menzel, W. P., Zhang, W., Sun, F., Schmit, T. J., Gurka, J. J., and Weisz, E.: Synergistic use of MODIS and AIRS in a variational retrieval of cloud parameters, J. Appl. Meteorol., 43, 1619–1634, 2004.

Maddy, E. S., Barnet, C. D., Goldberg, M., Sweeney, C., and Liu, X.: CO_2 retrievals from the Atmospheric Infrared Sounder: Methodology and validation, J. Geophys. Res., 113, D11301, doi:10.1029/2007JD009402, 2008.

Moody, E. G., King, M. D., Schaaf, C. B., and Platnick, S.: MODIS-derived spatially complete surface albedo products: Spatial and temporal pixel distribution and zonal averages, J. Appl. Meteor. Climatol., 47, 2879–2894, 2008.

Morino, I., Uchino, O., Inoue, M., Yoshida, Y., Yokota, T., Wennberg, P. O., Toon, G. C., Wunch, D., Roehl, C. M., Notholt, J., Warneke, T., Messerschmidt, J., Griffith, D. W. T., Deutscher, N. M., Sherlock, V., Connor, B., Robinson, J., Sussmann, R., and Rettinger, M.: Preliminary validation of column-averaged volume mixing ratios of carbon dioxide and methane retrieved from GOSAT short-wavelength infrared spectra, Atmos. Meas. Tech., 4, 1061–1076, doi:10.5194/amt-4-1061-2011, 2011.

Noël, S., Buchwitz, M., Bovensmann, H., and Burrows, J. P.: Validation of SCIAMACHY AMC-DOAS water vapour columns, Atmos. Chem. Phys., 5, 1835–1841, doi:10.5194/acp-5-1835-2005, 2005.

Razavi, A., Clerbaux, C., Wespes, C., Clarisse, L., Hurtmans, D., Payan, S., Camy-Peyret, C., and Coheur, P. F.: Characterization of methane retrievals from the IASI space-borne sounder, Atmos. Chem. Phys., 9, 7889–7899, doi:10.5194/acp-9-7889-2009, 2009.

Rodgers, C. D.: Inverse Methods for Atmospheric Sounding: Theory and Practice, World Sci., Hackensack, N. J., 2000.

Rothman, L. S., Gordon, I. E., Barbe, A., Chris Benner, D., Bernath, P. F., Birk, M., et al.: The HITRAN 2008 molecular spectroscopic database, J. Quantitative Spectrosc. Rad. Transfer, 110, 533–572, 2009.

Saitoh, N., Imasu, R., Ota, Y., and Niwa, Y.: CO_2 retrieval algorithm for the thermal infrared spectra of the Greenhouse Gases Observing Satellite: Potential of retrieving CO_2 vertical profile from high-resolution FTS sensor, J. Geophys. Res., 114, D17305, doi:10.1029/2008JD011500, 2009.

Schmidt, U. and Khedim, A.: In situ measurements of carbon dioxide in the winter arctic vortex and at midlatitudes: An indicator of the "Age" of the stratosphere, Geophys. Res. Lett., 18, 763–766, 1991.

Scott, N. A.: A direct method of computation of transmission function of an inhomogeneous gaseous medium: description of the method and influence of various factors, J. Quant. Spectrosc. Radiat. Transfer, 14, 691–707, 1974.

Shephard, M. W., Herman, R. L., Fisher, B. M., Cady-Pereira, K. E., Clough, S. A., et al.: Comparison of Tropospheric Emission Spectrometer nadir water vapor retrievals with in situ measurements J. Geophys. Res., 113, D15S24, doi:10.1029/2007JD008822, 2008.

Stamnes, K., Tsay, S., Wiscombe, W., and Jayaweera, K.: Numerically stable algorithm for discrete-ordinate-method radiative transfer in multiple scattering and emitting layered media, Appl. Optics, 27, 2502–2509, 1988.

Worden, J., Kulawik, S., Shepard, M. W., Clough, S. A., Worden, H., Bowman, K., and Goldman, A.: Predicted errors of tropospheric emission spectrometer nadir retrievals from spectral window selection, J. Geophys. Res., 109, D09308, doi:10.1029/2004JD004522, 2004.

Worden, J., Kulawik, S., Frankenberg, C., Payne, V., Bowman, K., Cady-Peirara, K., Wecht, K., Lee, J.-E., and Noone, D.: Profiles of CH_4, HDO, H_2O, and N_2O with improved lower tropospheric vertical resolution from Aura TES radiances, Atmos. Meas. Tech., 5, 397–411, doi:10.5194/amt-5-397-2012, 2012.

Xiong, X., Barnet, C., Maddy, E., Sweeney, C., Liu, X., Zhou, L., and Goldberg, M.: Characterization and validation of methane products from the Atmospheric Infrared Sounder (AIRS), J. Geophys. Res., 113, G00A01, doi:10.1029/2007JG000500, 2008.

Yoshida, Y., Ota, Y., Eguchi, N., Kikuchi, N., Nobuta, K., Tran, H., Morino, I., and Yokota, T.: Retrieval algorithm for CO_2 and CH_4 column abundances from short-wavelength infrared spectral observations by the Greenhouse gases observing satellite, Atmos. Meas. Tech., 4, 717–734, doi:10.5194/amt-4-717-2011, 2011.

Yoshida, Y., Kikuchi, N., Morino, I., Uchino, O., Oshchepkov, S., Bril, A., Saeki, T., Schutgens, N., Toon, G. C., Wunch, D., Roehl, C. M., Wennberg, P. O., Griffith, D. W. T., Deutscher, N. M., Warneke, T., Notholt, J., Robinson, J., Sherlock, V., Connor, B., Rettinger, M., Sussmann, R., Ahonen, P., Heikkinen, P., Kyrö, E., Mendonca, J., Strong, K., Hase, F., Dohe, S., and Yokota, T.: Improvement of the retrieval algorithm for GOSAT SWIR XCO_2 and XCH_4 and their validation using TCCON data, Atmos. Meas. Tech., 6, 1533–1547, doi:10.5194/amt-6-1533-2013, 2013.